

Miniature Biplanar Coils for Alkali-Metal-Vapor Magnetometry


Michael C. D. Tayler^{1,*}, Kostas Mouloudakis¹, Rasmus Zetter^{2,3}, Dominic Hunter^{1,†}, Vito G. Lucivero¹, Sven Bodenstedt¹, Lauri Parkkonen^{2,3} and Morgan W. Mitchell^{1,4}

¹*ICFO—Institut de Ciències Fotòniques, The Barcelona Institute of Science and Technology, Castelldefels (Barcelona) 08860, Spain*

²*Department of Neuroscience and Biomedical Engineering, Aalto University School of Science, Aalto 00076, Finland*

³*MEGIN Oy, Helsinki 00530, Finland*

⁴*ICREA—Institut Catalana de Recerca i Estudis Avançats, Barcelona 08010, Spain*

 (Received 19 March 2022; revised 6 May 2022; accepted 13 June 2022; published 15 July 2022)

Atomic spin sensors offer precision measurements using compact microfabricated packages, placing them in a competitive position for both market and research applications. The performance of these sensors, such as the dynamic range, may be enhanced through magnetic field control. In this work, we discuss the design of miniature coils for three-dimensional localized field control by direct placement around the sensor, as a flexible and compact alternative to global approaches used previously. Coils are designed on biplanar surfaces using a stream-function approach and then fabricated using standard printed-circuit techniques. Application to a laboratory-scale optically pumped magnetometer of sensitivity approximately $20 \text{ fT}/\sqrt{\text{Hz}}$ is shown. We also demonstrate the performance of a coil set measuring $7 \times 17 \times 17 \text{ mm}^3$ that is optimized specifically for magnetoencephalography, where multiple sensors are operated in close proximity to one another. Characterization of the field profile using ^{87}Rb free-induction spectroscopy and other techniques show $> 96\%$ field homogeneity over the target volume of a MEMS vapor cell and a compact stray-field contour of approximately 1% at 20 mm from the center of the cell.

DOI: [10.1103/PhysRevApplied.18.014036](https://doi.org/10.1103/PhysRevApplied.18.014036)

I. INTRODUCTION

Atomic spin devices based on alkali-metal vapors are among the results of the “second quantum revolution” [1], pushing the boundaries of sensing and metrology. They have the potential to reshape technological solutions through ultraprecise clocks for timekeeping [2], magnetometers for geomagnetic and biomagnetic investigation [3,4], or gyroscopes for navigation and autonomous control [5,6]. The miniaturization and mass manufacturing of atomic devices is also a highly active area of research. So far, miniaturization has been addressed with etched silicon cells to encapsulate the alkali medium [7–9] and vertical cavity surface-emitting lasers (VCSELs) for optical pumping [10], both of which could be manufactured in large quantities at a competitive cost per unit.

In this paper, we consider the design and manufacturability of another important component of alkali-metal-based sensors: electromagnetic coils. Precisely controlled magnetic fields are central to the proper operation of

optically pumped magnetometers (OPMs); in particular, for the variety based on locking to the narrow ground-state Hanle resonance of the alkali-metal atoms around zero field [11–13]. Due to their simple optics and possibility for compact packaging, a few companies have produced commercial prototypes of such OPMs for single- or multisensor use [14,15]. These OPMs are competitive with superconductor-based magnetometers in many applications, at present including magnetoencephalography (MEG) [16], magnetocardiography [17], magneto-myography [18], and low-field nuclear magnetic resonance [19], among others.

Precise control of magnetic fields is required in almost every OPM application. First, as already mentioned, a uniform field may be required to maintain a desired field across the active volume of the vapor, whether that be for the Hanle resonance or for other magnetometers that operate at ambient field [20,21]. Similarly, the control of field gradients can be a critical factor in applications requiring high magnetic coherence. It is also advantageous to minimize stray fields when two or more sensor units are used in close proximity to one another. In the case of OPMs, a reduced stray field minimizes crosstalk and improves sensor dynamic range [22,23] and also ensures a linear

*michael.tayler@icfo.eu

†Present address: Department of Physics, SUPA, University of Strathclyde, Glasgow G4 0NG, United Kingdom

well-defined sensor readout [24]. Together, these requirements define a design goal for magnetic coils, which must be met by mass-manufacturing techniques.

Here, we discuss coil sets where electrical-current paths are confined to two parallel planes (i.e., biplanar coils) to provide magnetic fields along three orthogonal spatial directions. The biplanar geometry facilitates production using standard printed-circuit-board (PCB) techniques. Each current path is separately optimized via the stream-function method [25] to produce a homogeneous central field at the location of the alkali-metal sensor. As a case study, we demonstrate a miniature biplanar coil set designed to be used with a microelectromechanical systems (MEMS) atomic vapor cell, where the coils must have a stray field below 1%–2% at 20-mm distance to minimize crosstalk between sensors. A larger coil set, inexpensively manufactured on a flexible PCB, is also designed to retrofit an existing laboratory OPM setup.

The paper is organized as follows. Sec. II summarizes the design criteria for OPM-motivated biplanar coils using a simple theory of zero-field OPMs and then a coil design work flow based on the stream-function optimization method. The results given in Sec. IV validate the resulting design specification, first by quantifying the magnetic inhomogeneity at the coil center and then by mapping the stray field to deduce the crosstalk performance. Application to magnetometry is also demonstrated, where coils and the MEMS cell form part of a zero-field OPM with open-loop sensitivity $20 - 40 \text{ fT}/\sqrt{\text{Hz}}$.

II. THEORY

A. Near-zero-field OPM response

Alkali vapors exhibit various nonlinear effects near atomic absorption resonances, such as optical pumping, magneto-optical rotation [26], and optical transparency [27], which may be utilized for metrology purposes, including magnetometry. Commercial OPMs produced so far for MEG are based on the ground-state Hanle effect, which refers to a magnetic-field-dependent absorption of circularly polarized light by alkali atoms [28–30]. The characteristics of the effect are: (i) maximum transmission of light through the atomic vapor at zero field $\mathbf{B} = (B_x, B_y, B_z) = \mathbf{0}$ when atoms are pumped to saturation; and (ii) for light propagation along the z axis, an approximately Lorentzian dependence of transmission versus B_x or B_y , which we quantify using the B_x field, giving half-maximum transmission, $B_x = B_1$.

It is common to detect the Hanle resonance using quadrature demodulation [31] of the transmission signal when an oscillating transverse field $\mathbf{B}_{\text{mod}}(t) = (B_{\text{mod}} \cos(\omega_{\text{mod}} t), 0, 0)$ is applied, with $B_{\text{mod}} \sim B_1$. The dynamics of the atomic spin polarization vector $\mathbf{P} = (P_x, P_y, P_z)$ under \mathbf{B} and \mathbf{B}_{mod} can be described by the Bloch equations [32,33]. This is studied by Iivanainen

et al. [22], from which we derive the results below. If the total magnetic field is $\mathbf{B}_{\text{total}}(t) = \mathbf{B}_{\text{mod}}(t) + \mathbf{B}_0 + \delta\mathbf{B}$, where \mathbf{B}_0 , $|\mathbf{B}_0| \ll B_1$, is the nominal field and $\delta\mathbf{B}$, $|\delta\mathbf{B}| \ll |\mathbf{B}_0|$, is a small deviation to be measured, then defining, for convenience, $\beta_\alpha \equiv B_\alpha/B_1$, the phase quadrature of P_z is

$$\tilde{P}_z = P_z^{(0)} J_0(p) J_1(p) \mathbf{c} \cdot \delta\boldsymbol{\beta} + O(\delta\boldsymbol{\beta})^2, \quad (1)$$

where $P_z^{(0)}$ is the steady-state spin polarization that optical pumping would produce at zero field, $p = |B_{\text{mod}}/B_1|$, and $\mathbf{c} = (c_x, c_y, c_z)$ is the first-order responsivity, scaled such that $\mathbf{c} = (1, 0, 0)$ at $\mathbf{B}_0 = \mathbf{0}$. The components of \mathbf{c} are

$$c_x = \frac{1}{1 + \beta_x^2} \left(1 - J_0^2(p) \frac{\beta_z^2 + \beta_y^2}{1 + \beta_x^2} \right), \quad (2a)$$

$$c_y = \frac{-J_0^2(p)}{1 + \beta_x^2} \left(\beta_z + 2 \frac{\beta_x \beta_y}{1 + \beta_x^2} \right), \quad (2b)$$

$$c_z = \frac{-J_0^2(p)}{1 + \beta_x^2} \left(\beta_y + 2 \frac{\beta_x \beta_z}{1 + \beta_x^2} \right). \quad (2c)$$

Equation (1) is convenient because it allows us to separate $\delta\boldsymbol{\beta}$, the signal that we want to measure, from $\boldsymbol{\beta}$, the background field. First, the amplitude of the quadrature signal is highest for $\beta_x = 0$, thus motivating operation as close to zero field as possible. As shown in Fig. 1, a field bias $\mathbf{B}_0 \neq \mathbf{0}$ produces various changes in the responsivity, relative to the ideal zero-field condition. The on-axis component β_x reduces the desired response c_x . The off-axis components β_y and β_z produce both a reduction of c_x and an increase in the undesired components c_y and c_z . Such distortions, both in the magnitude and direction of the responsivity, can have a significant impact on the quality of MEG reconstruction [34].

The spatial homogeneity of \mathbf{B} is also important. Most immediately, inhomogeneity of \mathbf{B}_0 within the active volume implies that different locations experience different responsivities \mathbf{c} . Due to the negative curvature of c_x with respect to each component of $\boldsymbol{\beta}$, inhomogeneity generically implies a reduction in the volume-averaged c_x relative to c_x at the center of the active volume. The magnitude of this effect can be roughly estimated by comparing the gradient to B_1 divided by the linear dimension of the active volume, which is typically of the order 10 nT mm^{-1} . Second, since OPMs are densely packed in the MEG application, the field produced by one OPM at the location of its neighbors is naturally of concern. In this context, Eq. (2) can be used to find limits on acceptable stray fields.

Together, these zero-field conditions can be used to define constraints on the components of $\boldsymbol{\beta}$ for an OPM design.

B. Field control for zero-field OPMs used in MEG

In MEG, a few to a hundred zero-field OPM sensor modules are mounted in an array around a subject's head, with

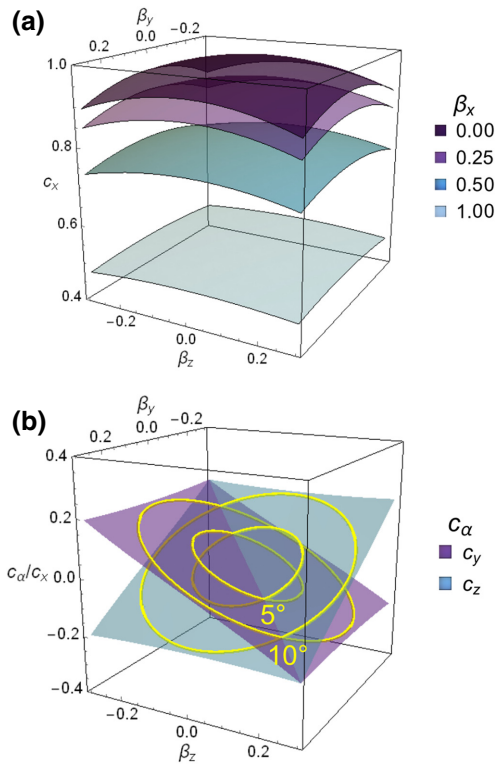


FIG. 1. The single-beam OPM-scaled responsivity \mathbf{c} versus the scaled bias field $\boldsymbol{\beta} \equiv \mathbf{B}_0/B_1$ from Eq. (2), with $p = 1$: (a) the response coefficient c_x versus β_y and β_z at fixed β_x ; and (b) the sensitive axis perturbations c_y/c_x and c_z/c_x versus β_y, β_z at fixed $\beta_x = 0$. Yellow contours indicate a tilt of \mathbf{c} away from the x axis.

the aim of mapping the magnetic field normal to the scalp surface. Dipole source localization based on inverse modeling of the surface field map requires the output of each OPM to be proportional to the normal field component [34,35], although a small time-independent component at each sensor is sometimes allowed, overall motivating the magnetic field over the entire array to be nulled as far as possible. At present, magnetically shielded rooms [14,36] or smaller person-sized magnetic shields [37,38] are used to passively attenuate background magnetic fields down to tens of nanotesla and then shim coils inside the shield may further cancel residual fields at the head position into a range where arrayed OPMs are operable.

Active field-control techniques have more recently shown the potential for great increase in the usability of OPM-based MEG. Also known as closed-loop OPM operation, these techniques calculate from the demodulation signal a compensatory x field that is fed back to the sensor in real time, giving $\beta_x = 0$ to ensure a proportional readout and also increase the sensor dynamic range. Field-feedback loops using large coils to compensate for drift in background fields over the entire sensor array have demonstrated improved operation in suboptimal shielding

[14,22,39,40] and improved “wearability” by ensuring linear signal output from OPM sensors while a subject’s head is in motion [41]. The global-control approaches demonstrated thus far using large single coils are, however, limited in temporal bandwidth and cannot fully null field gradients over the array [42].

A more comprehensive feedback solution with the potential to further extend the possible range of head movements or tolerate worse shielding and/or gradients is to locally null the field at each OPM sensor using a miniature set of coils. The main challenge of localized field control is to operate multiple field-feedback loops without introducing crosstalk. Here, the source of crosstalk is where a time-dependent compensatory field at one OPM sensor is noncompensatory at its neighbors and may significantly alter the measured magnetic field component [24]. At this point, the stray fields produced between neighboring OPMs become of concern and indeed may be considered the dominant source of error in the response. One strategy to mitigate crosstalk would be to limit stray fields from the local coils, so that these are small compared to $\delta\beta_x$; for instance, between two OPM sensors j and k , imposing a limit $|a_{k,x}^{(j)}\beta_x^{(k)}| \ll |\delta\beta_x^{(j)}|$, where $\delta\beta_x^{(j)}$ is the target field measured at j , $\beta_x^{(k)}$ is the feedback field at k , and $a_{k,x}^{(j)}$ is the fraction of $\beta_x^{(k)}$ seen at j . A reasonable limit based on values $\delta B_x \sim 10$ pT, a typical line width of $B_1 \sim 10$ nT, and the assumption that the OPMs are all modulated in phase would be $a < 0.01$ between adjacent sensors in the array.

C. Coil optimization via stream-function method

In principle, OPM crosstalk can be completely avoided by suitable coil design. Magnetostatics allows a current distribution to produce a uniform field with zero gradient and a zero fringing field; for example, the so-called “fluxball” current geometry [43]. In practice, good approximations to this ideal can be produced, even given geometrical constraints such as confinement of the currents to application-defined surfaces [44] (e.g., printed circuits).

In this work, we employ a stream-function method [25] to find current densities that best satisfy the constraints imposed. Specifically, we use the implementation described by Zetter *et al.* [44,45] to find line-current paths on planar two-dimensional surfaces for PCB fabrication. The first step of the method is to define the surface regions upon which currents can be placed. Constraints related to the surface current are also defined, such as components of the magnetic field at positions inside and outside the surface or constraints related to eddy currents as well as high-permeability shielding in the vicinity of the coil structure. The next step involves discretizing a current density function on the surface using a triangle mesh and then, finally, numerically optimizing the current density against

an objective function to find the best discrete current pattern fulfilling the constraints. Typically, the objective is to minimize either the inductance or the resistance of the surface current.

III. METHODS

A. Coil design and fabrication

1. Oversize coils

Continuous surface-current densities on biplanar surfaces are separately optimized for each X, Y, and Z coil using the “BFIELDTOOLS” software package [44,45]. The field specification used in the optimization of each coil consists of a target field specification and a stray-field specification. For the target field, a homogeneous field with $< 0.25\%$ error per field component is specified within a spherical volume of 2-mm radius located halfway between coil planes. The region is discretized on a Cartesian grid with 12 points along each axis, discarding points further than 2 mm away from the grid center to attain the spherical shape. For the stray-field specification, less than 2% of the target field (for each field component) is allowed at the surface of a cylinder with an inner diameter of 140 mm and a length of 160 mm. The cylinder is also centered on the grid and represents the internal dimensions of the magnetic shield in which the OPM oven is to be mounted. In practice, this stray-field constraint has minimal effect on the design.

Continuous surface-current densities on the coil planes are optimized using a minimum-inductance objective. For each coil, the optimized surface-current density is then discretized into individual current loops by extracting a number of equally spaced isosurfaces from the scalar stream function. The number of isosurfaces directly translates into the number of coil windings; a larger number means that the discretized current better approximates the continuous current density and also yields a higher field-to-current ratio, but also results in tighter spacing between loops. The

isosurface number is chosen heuristically by weighing the desired field parameters against manufacturability. For the Y and Z coils, the number is 6, while for the X coil, the number is 8.

The set of coils is optimized initially using interplane distances of a four-layer 1.6-mm-thickness FR4 fiberglass PCB; the design is changed midprocess, however, to an all-in-one flexible two-layer PCB. The flex design is chosen to facilitate installation on the OPM oven setup by avoiding the need to manually install connection wires between the planes and also because of lower fabrication costs.

Current paths for each coil are then assigned to top or bottom layers of a two-layer PCB as 0.15-mm-wide traces using a standard PCB-layout editor software program (KiCAD). Connecting wires between each coil loop are manually routed and extra out or return wire paths are kept spatially close together to maintain faithfulness to the intended magnetic field profile to the maximum extent. Connections between layers (vias) and breakout solder pads are also manually placed. The lower layer of the X coil is manually modified by adjusting the radius of the innermost current loop to accommodate the manufacturing of all four coils on a two-layer PCB. This *post hoc* modification is expected to slightly affect the field-to-current ratio without significantly affecting the field homogeneity. A Helmholtz coil (XH) with principal axis along the x direction is also routed on the two-layer PCB.

Exported design files (GERBER format) are then sent to a PCB fabricator (PCBway, Shenzhen, China), for production of the coils on a 0.2-mm-thick flexible polyimide substrate [Fig. 2(a)].

2. Miniature coils

The miniature coil system is designed for a compact mass-manufacturable OPM. The biplanar coils as illustrated in Fig. 2(b) comprise two stacks of square planes on either side of a cylindrical target region corresponding to the intended position of a MEMS atomic vapor cell,

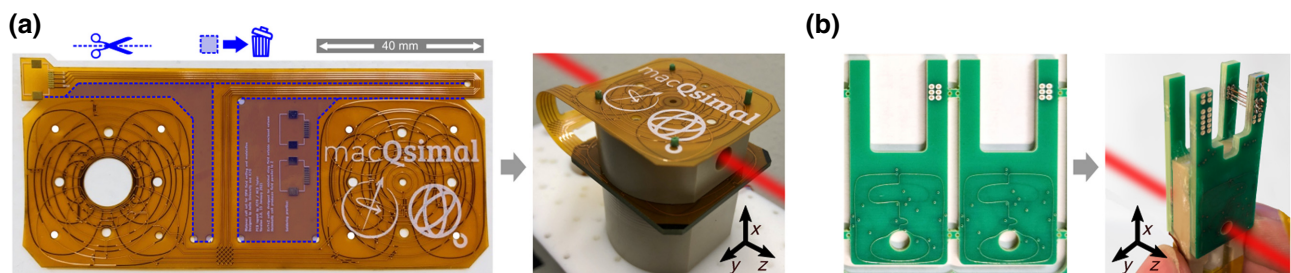


FIG. 2. Photographs of miniature PCB coil sets as received from the manufacturer and when integrated into the OPM oven setup. (a) A flexible two-layer PCB biplanar coil comprising the three high-homogeneity coils (X, Y, Z) and a Helmholtz coil along the x direction (XH). The small circular holes in the board are used for alignment and mounting, while the large hole accommodates the OPM heater element. The distance between the two coil planes is 15 mm. (b) Multilayer FR4 PCB with interplane distance of 6.3 mm, comprising three coils (X, Y, Z) optimized for minimal stray field.

of diameter 3.1 mm and thickness 1.5 mm. The upper and lower coil plane stacks are +3.5 mm and −2.8 mm from the target-region center, respectively, and have a size of $17 \times 17 \text{ mm}^2$. The symmetry axis of the cylinder is located at a distance of 4.5 mm from the edge of the coil surfaces to reduce sensor standoff distance in the target OPM.

Current densities are optimized under a stray-field constraint specified as 2% on a cylindrical surface grid centered on the target region, of length 30 mm and radius 20 mm. Unlike the oversize coils, the stream-function optimization is performed using a minimum-resistance quadratic objective in order to maximize the smoothness of the current patterns. Furthermore, the discretization from continuous surface-current density to discrete current isosurfaces is manually optimized to ensure the best balance between performance and manufacturability; instead of choosing an integer N of equally spaced isosurfaces, discretized coil candidates are generated by choosing every L_{th} isosurface from a set of LN equispaced isosurfaces. Coil candidates are generated for $N = [6, 8, 10]$ and $L = [1, \dots, 16]$. Finally, the candidate with the best combination of homogeneity and stray field is chosen, subject to a minimum trace spacing of 0.15 mm.

Like the oversize coils, current paths for each coil are then imported into a PCB layout editing software program (KiCAD) and assigned to different layers of a multilayer PCB. Connecting wires between each coil loop, connections between wires, and breakout solder pads are manually routed. The design is finally manufactured on a standard FR4 PCB substrate (Multi Leiterplatten GmbH, Brunthal-Hofolding, Germany).

B. Test-setup components

1. Atomic cell and oven

The biplanar coils are tested in laboratory environment as part of a zero-field-resonance OPM. A 1.5-mm-thick MEMS vapor cell containing ^{87}Rb and N_2 buffer gas (CSEM, Neuchâtel, Switzerland) is placed in a slotlike cavity inside a ceramic oven (Shapal Hi-M soft) of diameter 15 mm and height 15 mm. The flexible biplanar PCB coil set is attached to the top and bottom faces of the oven. Protruding from the base of the oven along the x axis is a cylindrical ceramic pillar of height 20 mm and diameter 8 mm. The pillar is wrapped with nichrome wire to provide resistive ac heating: a mean electrical power of 10 W at approximately 30 kHz heats the oven to a temperature above 150 °C. A hole is also made through the top part of the oven along z to allow the laser beam to pass. This assembly is contained inside a polyetheretherketone (PEEK) structure, as illustrated in Fig. 2(a), for mechanical support and additional thermal insulation.

2. Magnetic shield

All measurements using the atomic vapor cell, cell oven, and biplanar coils are made inside a four-layer mu-metal shield (Magnetic Shields Ltd., United Kingdom). The thermal magnetic noise of the shield is approximately $12 \text{ fT}/\sqrt{\text{Hz}}$ at 20 Hz and the residual dc field along each axis is below 50 nT. No other coils, except for the local biplanar coils placed around the oven, are present inside the magnetic shield.

C. Free-induction-decay measurements

The magnetic field-to-current ratio and field homogeneity generated across the target region of each biplanar coil are determined by measuring the free precession of optically polarized ^{87}Rb in the MEMS vapor cell.

A single elliptically polarized beam of wavelength near to the ^{87}Rb D_1 line is used to optically pump and probe the atoms [46]. The beam is sourced from a DBR laser located outside the magnetic shield, while the coils and oven assembly are placed inside the shield. The pulse sequence shown in Fig. 3(a) shows the temporally separated pump and probe stages of the measurement. During optical pumping, a magnetic field of 300 nT along x is applied and the laser frequency is modulated at the Larmor frequency to resonantly drive atomic coherence [47–49], producing a component of atomic polarization orthogonal to the beam propagation axis. The magnetic field is then rapidly switched to a field \mathbf{B}_0 , the major component of which is along one of the x , y , or z axes, and the free precession is probed via the time-dependent optical rotation induced in the linearly polarized component of the laser beam. A balanced photodetector (Thorlabs PDB450A) connected to a digital-acquisition card (NI-DAQ PCI-4462) is used to record the intensity of the s and p polarization components.

For each coil, the linear slope of the free-induction-decay (FID) frequency is measured versus the applied current and divided by the atomic gyromagnetic ratio ($\gamma/(2\pi) = 7.0 \text{ Hz nT}^{-1}$) to yield the field-to-current ratio.

D. Stray-field mapping

Stray magnetic field profiles are measured with a commercial self-contained OPM (Quspin model QZFM2 Zero-Field Magnetometer) placed at different positions in the region outside the coil planes. Alternating magnetic fields of approximately 2 nT are applied to each biplanar coil at a fixed frequency in the range 10–20 Hz. The OPM-sensor output is sampled for 30 s and then Fourier transformed to separate the signals corresponding to each coil. The signal amplitudes at each frequency are scaled to the response of a known test field, in order to convert each stray-field value into a percentage of the field at the coil center.

For the case of the oversize coils, the OPM is placed on a three-axis translation stage and stray field along the x axis

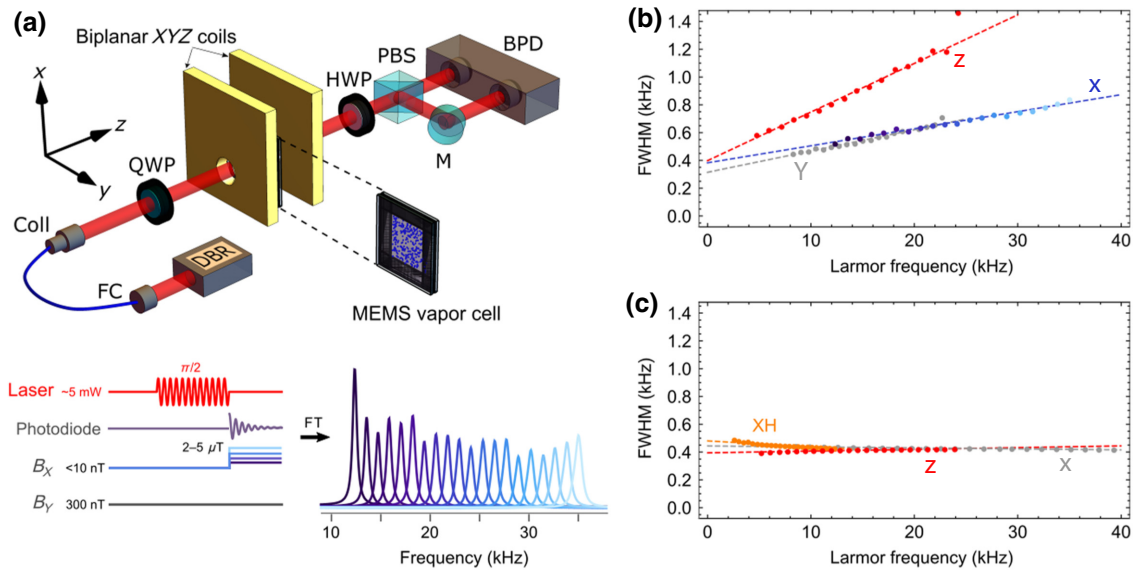


FIG. 3. The free-induction spectroscopy of ^{87}Rb in a MEMS vapor cell versus the local magnetic field supplied by biplanar coils. (a) The optical setup for measurement of atomic spin precession and transverse relaxation rates: DBR, distributed Bragg reflector laser; FC, fiber collimator; QWP (HWP), 795-nm quarter- (half-) wave plate; PBS, polarizing beam-splitter cube; M, mirror; BPD, balanced photodiode-pair detector; FT, Fourier transformation. (b) The spectral broadening of the magnetic resonance line versus the atomic Larmor frequency for magnetic fields applied in each miniature coil: X (long axis, blue), Y (short axis, gray), and Z (laser beam axis, red). The inhomogeneous broadening per unit magnetic field corresponds to the gradient of each best-fit straight line, which equals the ratio of the gradient to the applied magnetic field for the corresponding coil: $\kappa = |\delta B/B_0|$ (where $\kappa_X = 1.2\%$, $\kappa_Y = 1.5\%$ and $\kappa_Z = 3.5\%$). (c) The field dependence of the transverse relaxation rate for the oversized coils. FWHM, full width at half maximum.

is measured in point-by-point fashion on a 2.5-mm grid in the x - y plane. For the case of the miniature coils, the OPM position inside the magnetic shield is fixed while the coils are moved on a grid corresponding to 2-mm translation along and 45° rotation about the x axis.

E. Single-beam OPM

Circularly polarized light of around 1 mW optical power at 795 nm is collimated, passed through a hole in the magnetic shield, and then through the MEMS vapor cell. The beam source as a VCSEL and the beam is conditioned using (in order) a Keplerian beam expander, a linear polarizer, and a zero-order quarter-wave plate. The transmitted beam is finally detected outside the shield using an amplified Si photodetector (Thorlabs model PDA36A2).

The laser wavelength for optical pumping depends on the pressure-shifted atomic resonance frequency and is tuned on resonance by minimizing the transmission of circularly polarized light when a large transverse dc field of the order of $10 \mu\text{T}$ is applied to the atoms. The residual magnetic field is then nulled by applying direct current to the biplanar coils. A three-channel low-noise current source (Twinleaf CSB-10) is used to supply current to each coil through a 500Ω shunt resistor.

To null the background field, optical transmission measurements are performed around the zero-field Hanle

resonance. A slow (5 Hz) linear current ramp is applied to the X coil, to produce a field from $B_x = -250$ nT to $+250$ nT and the zero-field resonance corresponding to maximum transmission of light through the vapor is resolved to a line width of a few tens of nanotesla. The slow scan ensures that atomic polarization is in an approximately steady state during the sweep. From the resonance curve, a “sharpness” figure of merit is calculated, equal to the maximum transmission amplitude divided by the full-width-at-half-maximum (FWHM) transmission.

Currents of the order of 2–3 mA are applied to the Y and Z coils (I_y and I_z). An automated grid search produces a three-dimensional plot of (I_y, I_z, S) with a field resolution of 100×100 pT, thus giving the optimal nulling field as the point of highest sharpness. The procedure is iterated one or two times more, starting from the best-guess zero field, but this step is usually unnecessary.

To perform field modulation and demodulation operations, a commercially available audio codec chip (Cirrus Logic CS4272) is interfaced with a low-cost microcontroller unit (ARM Cortex M7 model IMXRT1060, CPU speed 600 MHz, 64-bit math) via an Inter-IC Sound (I^2S) bus. The outgoing I^2S signal from the microcontroller produces a sinusoidal voltage output of the codec (24 bit), to modulate the magnetic field produced by the X coil. The incoming I^2S signal is the ac-coupled signal, output from the amplified photodiode and digitized by the codec (24

bit). The incoming signal is digitally demodulated against the modulation frequency on board the microcontroller and low-pass filtered using a double-cascaded second-order biquad filter, and then the in-phase part of the signal [proportional to Eq. (1)] is sampled at 3 ksamples/s and output to a personal computer.

IV. RESULTS

A. Coil specification

Two biplanar XYZ coil sets are presented in this work, as follows.

1. Oversize coils

A three-axis biplanar coil system is designed to be fabricated on a PCB and retrofitted to an existing laboratory OPM setup where miniaturization is not a primary concern. Shown in Fig. 2(a), the coil system comprises two 40×40 -mm planes printed as a two-layer PCB on a single sheet of flexible polyimide, which is cut as indicated and then folded in half to give a 15-mm interplane distance. The support structure for the PCB is a plastic oven cavity containing a MEMS vapor cell of ^{87}Rb with approximate xyz dimensions $5 \times 5 \times 1.5 \text{ mm}^3$ [8]; the coils are therefore an order of magnitude larger than the MEMS cell and described as “oversize.” The coil planes include holes for screws and alignment rods as well as a large central hole in one of the planes for the vapor cell and heating element, which the PCB design has to accommodate.

The field specification for the oversize coils is as follows: (1) a homogeneous magnetic field over the volume occupied by the MEMS vapor cell, specified as $< 0.25\%$ error per field component in a spherical target region of radius 2 mm at the coil center, equidistant between the coil planes; (2) below 2% stray field at the inner walls of the commercial magnetic shield in which the OPM is placed; and (3) a target field-to-current ratio for each coil of between 100 and 200 nT mA $^{-1}$ (see the design details given in Sec. III). The final coil design includes coils for fields along the x (X coil), y (Y coil), and z (Z coil) axes plus a Helmholtz coil along the x axis (XH coil).

2. Miniature coils

Another three-axis biplanar coil system is designed for an ultracompact self-shielded zero-field OPM package to be used in MEG studies. For this design, small-form-factor coils are required to produce highly homogeneous magnetic fields at the vapor cell with minimal stray field outside the package. Additionally, coil placement is secondary to the placement of other components in the OPM, such as optics and thermal insulation. The geometric specification is thus a system comprising two planes on either side of a cylindrical target region of diameter 3.1 mm and thickness 1.5 mm, corresponding to the MEMS atomic vapor cell [8],

and an overall PCB footprint of $17 \times 17 \text{ mm}^2$ excluding connecting wires. The field specification is as follows: (1) 0.5% inhomogeneity per x , y , and z field component within the target region; and (2) a stray field, again for each field component, below 0.5% of the target field at 20-mm distance from the homogeneous target region. Orthogonality of the miniature coils is also well controlled. The computed mean angular distances between the three coils are in the range 89.7° to 90.6° . The manufactured PCB and assembled coils are shown in Fig. 2(b) (see the design and optimization-process details given in Sec. III).

B. Field-to-current ratio and homogeneity

The specification of the magnetic field inside the biplanar coils is validated through atomic FID measurements. As shown in Fig. 3(a) and described in Sec. III, a MEMS ^{87}Rb vapor cell is placed at the intended location in the center of the coil assembly and illuminated with D_1 laser light to produce atomic polarization. The atomic polarization is then allowed to precess in the magnetic field supplied by the coils and its magnetic moment along the beam axis is detected by Faraday rotation in the same laser beam. The rotation signal is proportional to $\exp(-R_2^*t)(B_x, B_y, 0) \cos(2\pi f_L t)/|\mathbf{B}|$. In this expression, \mathbf{B} is the average magnetic field over the volume where the beam intersects the atoms, $2\pi f_L \equiv \gamma|\mathbf{B}|$ is the atomic Larmor frequency, and R_2^* is the transverse relaxation rate.

Measurements of the Larmor frequency for a set of applied currents, such as those shown in the lower part of Fig. 3(a) for the X coil, allow precise estimation of the field-to-current ratio by fitting the derivative term in $B_\alpha = (\partial B_\alpha / \partial I_\alpha) I_\alpha$ with $\alpha \in \{x, y, z\}$. Experimental values of $\partial B_\alpha / \partial I_\alpha$ for both oversize and miniature coil systems are shown in Table I. Overall, there is good agreement between the experimental values and those predicted by the stream-function method during the design phase (also shown in Table I), particularly for the miniature coil set, where deviations are below 1%. The deviation between experimental and predicted values for the oversize coil set are slightly higher, at 2%–4%, which may be attributed to the design modification needed to accommodate all coil traces on the two-layer flexible PCB substrate.

The relaxation rate R_2^* is obtained from the FWHM ($\Delta\nu$, in hertz) of the Fourier-transformed FID signal, $R_2^*/\pi = \Delta\nu$, and provides direct information on the field inhomogeneity across the target region of the vapor cell. We can write $R_2^* = R_2 + R'$, where R_2 is the homogeneous relaxation rate including spin-exchange, spin-destruction, and optical-pumping relaxation effects, and R' is the rate of inhomogeneous broadening, which is linearly proportional to the gradient. To avoid compromising the OPM performance, gradients across the sensor atoms should be low enough to ensure that $R' \ll R_2$. Here, we quantify the field inhomogeneity through a derivative

TABLE I. The computed and FID-measured internal magnetic field parameters for the oversize- and miniature-coil systems. The computed field-to-current values refer to the sensitive volume of a MEMS vapor cell at the coil centers and are thus directly comparable to the FID values. The computed inhomogeneities are the 95th percentile of the field deviation over the MEMS cell, while the experimental value is obtained from the slope of the transverse relaxation rate versus the Larmor frequency for each series of FIDs.

	Coil	Field-to-current ratio (nT mA ⁻¹)		Inhomogeneity (%)	
		Computed	Experimental	Computed	Experimental
Miniature	X	180.1	179.1	1.1	1.2
	Y	119.3	115.7	1.3	1.5
	Z	184.5	184.1	2.4	3.5
Oversize	X	194.37	192.6(3)	0.55	< 0.1
	Y	112.43	116.3(2)	0.48	< 0.1
	Z	112.38	116.26(16)	0.46	< 0.1
	XH (Helmholtz)	59.16	60.1(1)	0.01	< 0.1

$\kappa_\alpha = \partial R_2^*/(\pi\gamma\partial B_\alpha) \equiv \partial\Delta\nu/\partial f_L$ for each coil, by assuming that $\kappa_\alpha = |\Delta B_{0,\alpha}/B_{0,\alpha}|$, where $\Delta B_{0,\alpha}$ is the effective variation in the magnetic field over the cell volume at a given B_0 along axis α . Values of $\Delta B_{0,\alpha}$ are determined in a similar way to the field-to-current ratios, by collecting a series of FID spectra for different applied currents and fitting the slope of $\Delta\nu$ versus f_L .

Experimental FID line widths obtained using the miniature coil set are shown in Fig. 3(b) and similarly using the oversize coil set in Fig. 3(c). The miniature coil set yields values of $\kappa_x = 1.2\%$, $\kappa_y = 1.5\%$, and $\kappa_z = 3.5\%$, while for the oversize coil set, κ_x , κ_y , and κ_z are all below 0.1%. It is unsurprising to find that the miniature biplanar coils produce fields with lower homogeneity than the oversize counterparts. The target volume of the miniature coils occupies a larger percentage of the overall coil and therefore imposes a greater challenge for the design optimization. Furthermore, in this case study, higher priority is given during the design phase to the minimization of stray fields. The smaller coil size is also more susceptible to errors in the interplane distance and plane alignment made during coil assembly. However, despite these trade-offs, the inhomogeneity remains relatively small and within 10% of the values expected for the design.

The relaxation data in Figs. 3(b) and 3(c) can also suggest limits imposed on the OPM dynamic range by field gradients. If the noise is limited by atomic spin projection noise, for example, the sensitivity will become significantly degraded above fields where R' becomes of the order of R_2 , or about 20 kHz Larmor frequency (30 μ T field) for the miniature X coil. For the oversize coils, the limit should occur at much higher field, because there is no noticeable slope of the relaxation rate versus the applied field.

C. External-field characterization

The fringe-field specifications of the two biplanar coils designs are also validated by comparing the experimental data with the simulation results. The BFIELDTOOLS

software package provides a convenient route to calculate the field profile from the optimized current paths, using a single built-in function. Three-dimensional representations of the stray field can then be plotted and inspected; for instance, the isosurface maps as plotted in Fig. 4, to show surfaces of constant stray-field magnitude. The isosurfaces in Fig. 4 indicate the stray field between 5% (red) and 0.1% (gray) of the field at the coil center. The overall most compact isosurfaces occur for the miniature Z coil, where the total field does not exceed 0.1% at any point further than 30 mm from the coil center.

In practical applications where it may be important to control external stray fields, usually only a small portion of the field map is relevant. Examples would be known positions where neighboring sensors are to be placed, or of predicted field hot spots. In these cases, the task of comparing experimental versus calculated fields then becomes a lower burden (especially where multiple prototypes are to be tested) because experimental field mapping only needs to be performed around the regions of practical concern. For example, in MEG, OPM sensors are typically arrayed on the head surface to measure the magnetic field component normal to the scalp [50]. If the magnetic field at each OPM sensor was supplied by the miniature coil set from Fig. 2(b), then x would be the field-sensitive axis and the nearest-neighbor sensors would lie in the y - z plane.

In this work, the fringe field of the miniature coils is validated on a cylindrical surface with radius $(y^2 + z^2)^{1/2} = 20$ mm and principal axis along x . The chosen value of 20 mm corresponds to a proposed minimum approach distance between vapor cells in a MEG array. As shown in Fig. 5(a) (see also Sec. III), specific components are experimentally mapped in point-by-point style by translating and/or rotating the coils with respect to an auxiliary OPM sensor (Quspin model QZFM2 Zero-Field Magnetometer) located in the fringe field. The orientation of the magnetometer is such that field components tangential to the cylinder surface are measured and the results are plotted in Fig. 5(b).

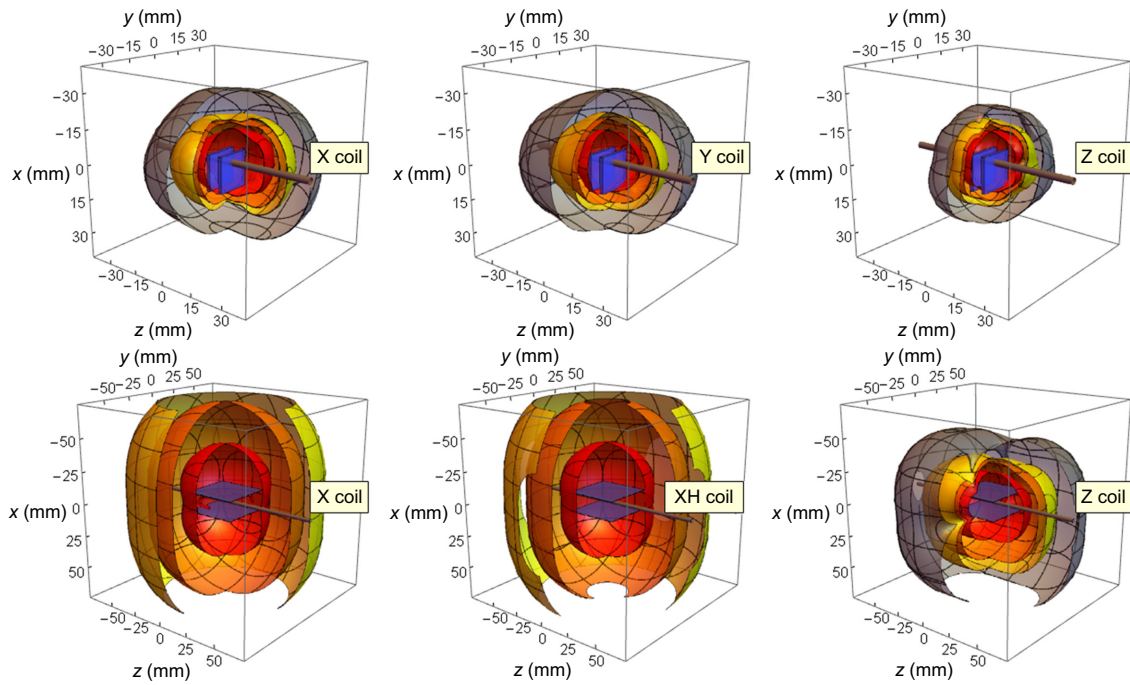


FIG. 4. Calculated stray-field maps for the miniature (top row) and oversize (bottom row) biplanar coils. The coil planes are indicated by blue shading and the intended path for a light beam is shown by the gray cylinder, which defines the z axis. The surfaces enclosed volume represent three-dimensional contours of decreasing total stray field; where visible within the plot range, the colors red, orange, yellow, and gray represent 5%, 1%, 0.5%, and 0.1% of the value of the field at the origin, respectively. The mesh lines correspond to the tick marks on the x , y , and z axes. The bottom row includes both the stream-function-optimized X coil and the Helmholtz coil XH. A plot for the oversize Y coil is not shown because after 90° rotation about x , it is equal to that for the Z coil.

Experimentally, the shape of the stray field contours agrees well with the BFIELDTOOLS simulations for all coils (shown in Fig. 4), and for the Y and Z coils the strength of the stray field also agrees quantitatively. For some

unknown reason, the stray fields of the X coil along the x' direction turn out to be much higher than expected, with a hot spot at the position $x = 7$ mm (235°) of around 1.2% experimental versus 0.3% computed. A partial

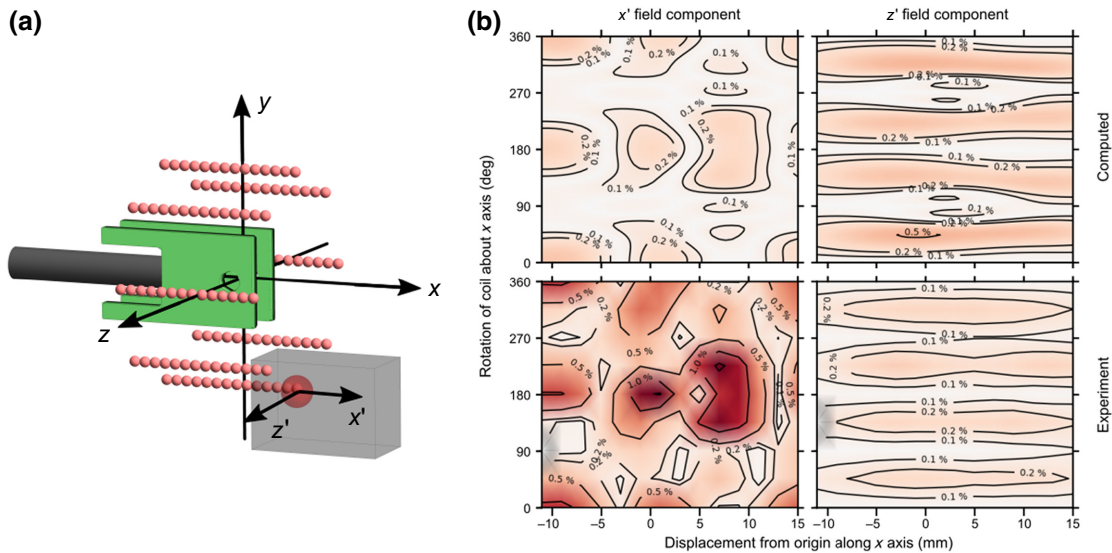


FIG. 5. Stray-field maps for the miniature X coil. (a) The experimental setup. Pink spheres indicate the location of the experimental data points in (b). (b) The computed and empirically measured magnitude of the stray-field components of the X coil along two axes tangential to the surface $\sqrt{y^2 + z^2} = 20$ mm.

reason for this result may be a small error in the inter-plane separation; coils misaligned by only 0.5 mm along the plane normal direction cause the computed stray field to reach around 0.5% at the 20-mm sensor standoff distance. In practice, the actual standoff distance may be less than the expected 20 mm due to imprecise sensor positioning and/or the finite width of the QZFM [51] vapor cell (approximately 1.5 mm diameter). Moreover, in practice, the QZFM sensitive axis is not exactly parallel to x' and additionally picks up around 20% of a large stray-field component along the radial y' direction. If the standoff distance is reduced to 18 mm, then the computed total field at the hot-spot location becomes of the order of 1% and therefore the experimental value of 1.2% could be explained by combined errors in coil alignment and sensor standoff of around 1 mm. Aside from the issue of alignment tolerance, the specific defect described here is highly localized, likely because the coil set is designed for minimal stray field on a spherical surface rather than on a cylinder and in some applications may not pose major problems. For example, it is possible to array the miniature coils on a square grid in the y - z plane at the 90° and 270° locations, which avoids the worst hot spots. In future, the design-optimization objective could be defined with a stronger stray-field constraint, including stray fields on multiple surfaces, to take tolerances into account and/or avoid local hot spots.

A validation of the stray field of the oversize coils is presented in Fig. 6. The contour plots show a field map generated using a similar procedure to that described above for the miniature coils but only the x component of the field is studied. The experimental stray fields of the X and Y coils along x are somewhat smaller than the corresponding computed results, by a factor of around 2. The field of the Z coil (not shown) along x' is roughly 10 times weaker than

that of the X coil, measuring around 1%–2% near to the coil plane and less than 0.1% upon moving 15 mm away from the plane, along x —which is expected, since the sensor axis is orthogonal to the principal axis of the coil. The stray-field map for the Y coil also reveals the symmetry plane along which the stray field is negligible ($< 0.1\%$).

Figure 6(b) also allows comparison between the fringe fields of the XH and X coils. The two maps are extremely similar to one another, which is in agreement with the computational prediction. The result is interesting because the single-loop XH coil takes up significantly less space on the PCB than the optimized X coil. In future, therefore, a smaller triple-coil set could easily be made on a two-layer flexible PCB, by using only the optimized Y and Z coils plus the XH coil.

D. Open-loop OPM performance

In each of the coil designs presented, the central homogeneous-field target region corresponds to the intended location of optically pumped atoms in a MEMS vapor cell. To provide a more complete characterization of the biplanar coil performance, we demonstrate a simple application of the system as a magnetometer.

We focus on a zero-field-resonance magnetometer comprising the MEMS vapor cell, the oven, and oversize PCB coils [Fig. 2(a)]. This assembly is placed inside a four-layer Mu-metal magnetic shield, while the laser source and other optical components to generate circularly polarized light are outside the shield and are fixed on an optical table, as detailed in Sec. III. The vapor-cell dimensions are identical to those used in the FID measurements presented in Sec. IV B. The vapor cell composition, however, is different, with the ^{87}Rb vapor density and the N_2 buffer gas pressure optimized to give the largest response of the

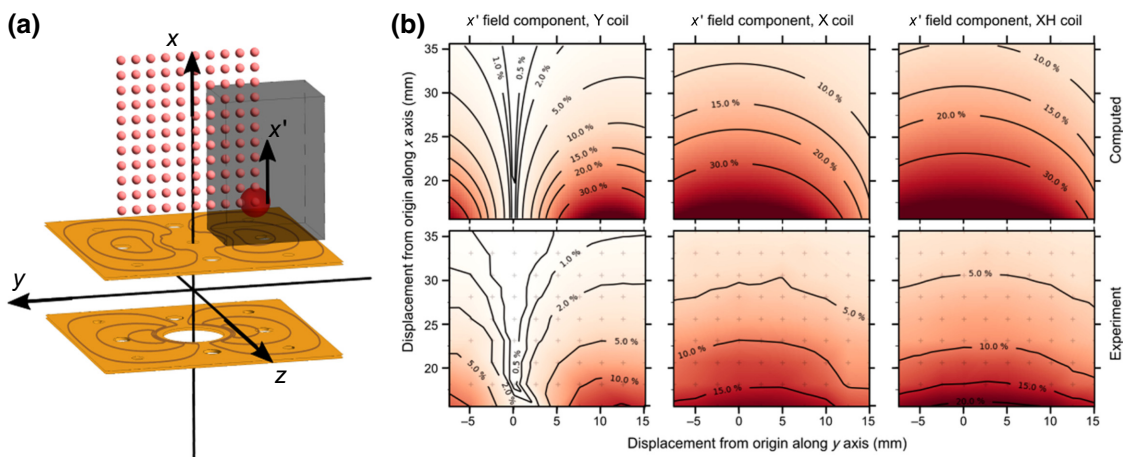


FIG. 6. Stray-field maps of the X, Y, Z, and XH oversize coils. (a) The experimental setup, showing the relative arrangement of the PCB planes and the magnetometer used to sample the x stray-field component in the x - y plane. The current loops for the biplanar Y coil are plotted in brown. (b) The computed and experimentally measured magnitude of the stray-field component along x . The pink spheres in (a) indicate the location of the experimental data points shown by crosses in (b).

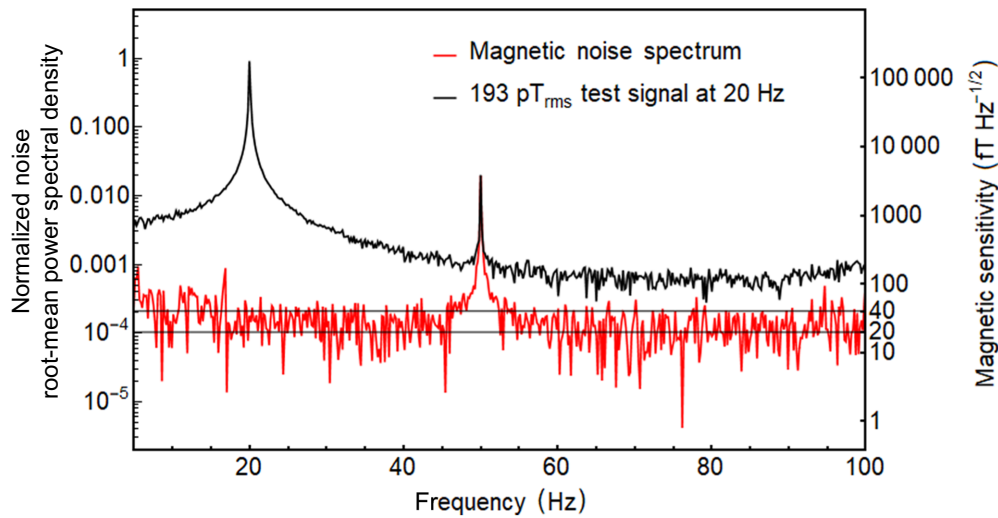


FIG. 7. A demonstration of zero-field-resonance magnetometry: open-loop magnetic noise spectra obtained using a MEMS ^{87}Rb vapor cell contained within the oven assembly of Fig. 2(a). A 533-Hz 24-nT modulation field is applied using the oversize X coil. The spectra are calculated as the root-mean power spectral density of the surplus optical-pumping light detected after the vapor cell and after demodulation, which we scale to a response curve for ac test signals of known amplitude in the range 1–200 Hz. The red curve indicates the noise background. The black curve is the response to a 20 Hz 193 pT_{rms} sinusoidal test signal applied in the X coil in addition to the modulation field.

quadrature signal [Eq. (1)] per unit field component B_x . The specific cell used has a zero-field resonance line width of $B_1 = 35$ nT and the best quadrature signal, empirically speaking, is obtained for modulation parameters $B_{\text{mod}} = 24$ nT and $\omega_{\text{mod}}/2\pi = 533$ Hz. The XH coil is used to provide the modulation field and the X, Y, and Z coils are used to null the total background field from several tens of nanotesla to below 5 nT. It is observed, as shown in Fig. 7, that the above settings can produce a demodulation signal with a field-equivalent baseline noise in the range of 20 fT/ $\sqrt{\text{Hz}}$ at frequencies of 20–100 Hz. The obtained sensitivity is similar to that of commercial-prototype OPMs that use miniature glass-cuboid [12] or etched-silicon MEMS [52–54] cells to contain the alkali medium, which reach of the order of 10–30 fT/ $\sqrt{\text{Hz}}$.

With regard to the noise floor in Fig. 7, it is estimated that the thermal noise of the magnetic shield contributes around 10 fT/ $\sqrt{\text{Hz}}$. System electronics excluding the VCSEL driver contribute an effective field noise of less than 2 fT/ $\sqrt{\text{Hz}}$. The VCSEL driver and other optical-noise sources are attributed to the remainder of the noise budget. A broader discussion of the MEMS magnetometer sensitivity, including results for the OPM in closed-loop mode and the miniature coils setup of Fig. 2(b), will be presented separately in an upcoming publication.

V. DISCUSSION AND CONCLUSIONS

Coil design is a multifaceted engineering task in which a large number of competing factors must be taken into

account and balanced, including size, geometry, field gradient, stray field, and manufacturability and cost. Classical coil designs such as Helmholtz coils can provide good performance but are not flexible in terms of their geometry and have a significant stray field. Sophisticated methods such as the stream-function coil-design framework applied in this work are required in applications with demanding geometrical and/or electrical constraints.

The miniature three-axis coil set designed in this work is intended to be positioned around an individual atomic vapor cell in an OPM array. The design specification of the OPM introduces significant constraints on the field profile both inside and outside the coil to minimize inhomogeneous broadening of the magnetic resonance line of the atoms and mitigate crosstalk fields, respectively. Given that planar PCB manufacturing is highly developed, scalable, and precise, the stream-function optimization framework applied on planar surfaces is especially suited to this design task, since the geometrical limitations of a planar structure can be compensated for by intricate in-plane current paths. Here, the specification of the miniature coils is experimentally validated as already close to the MEG design goal, even taking into account potential sources of error encountered experimentally, such as in the stray field.

In the future, improved planar coils could be made with additional design optimization. The effect of stray fields could be reduced by further scaling down coil size. For instance, the magnetic field at the center of a Helmholtz coil (defined by the loop radius and the inter-plane distance R) is proportional to $1/R$, while at displacements further than $\pm R$ along the main symmetry axis, the

magnetic field is proportional to R^2 . The scaling between the stray and the center field therefore goes as R^3 and coils printed directly onto the window substrate of the vapor cell may be an option [55], where permitted by the cell geometry and the aspect ratio. The Helmholtz coil is already close to optimal with regard to magnetic gradients because, by definition, the first nonzero derivative along the main axis (α) of the coil is $d^4 B_\alpha / d\alpha^4$. However, for a typical MEMS atomic vapor cell, where the beam direction z is perpendicular to the plane of the windows, a Helmholtz coil ($\alpha = z$) cannot provide the transverse modulation field (x) and therefore high-performance X- and Y-coil geometries must also be found. On the basis of the PCB trace width and the intertrace spacing alone, the coils presented in this work may be shrunk by a factor of 2–3 and still be manufactured using currently available PCB techniques (0.002 in. $\approx 50 \mu\text{m}$ minimum feature size); thus the biplanar design approach can, in principle, achieve lower stray fields by one order of magnitude. Potentially, such coils may address the secondary problem of crosstalk when the modulation fields of adjacent sensors is not exactly in phase, where the stray-field constraint is even tighter.

A smaller interplane spacing in the case of biplanar current surfaces would also help reduce the magnitude of fringe fields because the solid angle covered by the planes (as seen from the target region) can be increased. Another method would be to add one or more additional current layers, the main purpose of which is to create a self-shielded coil [56], e.g., a tetraplanar coil.

Finally, an alternative to the zero-field-operation requirement may be given by total-field OPMs that also reach high sensitivities [57,58] and can be miniaturized [3] but that implement complex optical configurations such as dual or multipass beams [59] and are partially limited by spin-exchange relaxation. An all-optical total-field OPM designed to eliminate sensor crosstalk has been demonstrated for MEG in an ambient (unshielded) environment [20], with a sensitivity reaching $15 \text{ fT}/\sqrt{\text{Hz}}$ in gradiometer mode ($10 \text{ pT}/\sqrt{\text{Hz}}$ single-sensor sensitivity). The utility of such OPMs in sensor arrays for MEG applications remains under study [60].

ACKNOWLEDGMENTS

The work was funded by: the European Union Horizon 2020 research and innovation programme under project macQsimal (Grant Agreement No. 820393); the Horizon H2020 Marie Skłodowska-Curie Actions projects ITN ZULF-NMR (Grant Agreement No. 766402) and PROBIST (Grant Agreement No. 754510); the Spanish MINECO project OCARINA (the PGC2018-097056-B-I00 project funded by MCIN/AEI/10.13039/501100011033/FEDER, “A way to make Europe”); the Severo Ochoa program (Grant No. SEV-2015-0522); the Generalitat de

Catalunya through the CERCA program; the Agència de Gestió d’Ajuts Universitaris i de Recerca under Grant No. 2017-SGR-1354; the Secretaria d’Universitats i Recerca del Departament d’Empresa i Coneixement de la Generalitat de Catalunya, cofunded by the European Union Regional Development Fund within the ERDF Operational Program of Catalunya (project QuantumCat, ref. 001-P-001644); the Fundació Privada Cellex; and the Fundació Mir-Puig. M.C.D.T. acknowledges financial support through the Junior Leader Postdoctoral Fellowship Programme from the “La Caixa” Banking Foundation (project LCF/BQ/PI19/11690021). We also thank Jacques Haesler, Sylvain Karlen, and Thomas Overstolz of the Centre Suisse d’Electronique et de Microtechnique SA (CSEM) in Neuchâtel (Switzerland) for supplying the MEMS vapor cells.

-
- [1] A. G. J. MacFarlane, J. P. Dowling, and G. J. Milburn, Quantum technology: The second quantum revolution, *Philos. Trans. R. Soc. London Ser. A: Math., Phys. Eng. Sci.* **361**, 1655 (2003).
 - [2] S. Knappe, V. Gerginov, P. D. Schwindt, V. Shah, H. G. Robinson, L. Hollberg, and J. Kitching, Atomic vapor cells for chip-scale atomic clocks with improved long-term frequency stability, *Opt. Lett.* **30**, 2351 (2005).
 - [3] P. D. D. Schwindt, S. Knappe, V. Shah, L. Hollberg, J. Kitching, L.-A. Liew, and J. Moreland, Chip-scale atomic magnetometer, *Appl. Phys. Lett.* **85**, 6409 (2004).
 - [4] D. Budker and M. Romalis, Optical magnetometry, *Nat. Phys.* **3**, 227 (2007).
 - [5] E. A. Donley, in *IEEE Sensors* (IEEE Sensors Conf., Waikoloa, Hawaii, 2010).
 - [6] M. E. Limes, D. Sheng, and M. V. Romalis, ^3He - ^{129}Xe Comagnetometry Using ^{87}Rb Detection and Decoupling, *Phys. Rev. Lett.* **120**, 033401 (2018).
 - [7] L.-A. Liew, S. Knappe, J. Moreland, H. Robinson, L. Hollberg, and J. Kitching, Microfabricated alkali atom vapor cells, *Appl. Phys. Lett.* **84**, 2694 (2004).
 - [8] S. Karlen, J. Gobet, T. Overstolz, J. Haesler, and S. Lecomte, Lifetime assessment of RbN_3 -filled MEMS atomic vapor cells with Al_2O_3 coating, *Opt. Express* **25**, 2187 (2017).
 - [9] J. Kitching, Chip-scale atomic devices, *Appl. Phys. Rev.* **5**, 031302 (2018).
 - [10] P. D. D. Schwindt, S. Knappe, V. Shah, L. Hollberg, J. Kitching, L.-A. Liew, and J. Moreland, Chip-scale atomic magnetometer, *Appl. Phys. Lett.* **85**, 6409 (2004).
 - [11] S. P. Krzyzewski, A. R. Perry, V. Gerginov, and S. Knappe, Characterization of noise sources in a microfabricated single-beam zero-field optically-pumped magnetometer, *J. Appl. Phys.* **126**, 044504 (2019).
 - [12] J. Osborne, J. Orton, O. Alem, and V. Shah, in *Proc. SPIE 10548*, edited by S. M. Shahriar and J. Scheuer, International Society for Optics and Photonics (Steep Dispersion Engineering and Opto-Atomic Precision Metrology XI, 2018), p. 89.

- [13] R. Slocum and B. Marton, Measurement of weak magnetic fields using zero-field parametric resonance in optically pumped ^4He , *IEEE Trans. Magn.* **9**, 221 (1973).
- [14] E. J. Pratt, *et al.*, in *Proc. SPIE 11700*, edited by S. M. Shahriar and J. Scheuer (Optical and Quantum Sensing and Precision Metrology, 2021), p. 1170032.
- [15] D. Sheng, A. R. Perry, S. P. Krzyzewski, S. Geller, J. Kitching, and S. Knappe, A microfabricated optically-pumped magnetic gradiometer, *Appl. Phys. Lett.* **110**, 031106 (2017).
- [16] S. Baillet, Magnetoencephalography for brain electrophysiology and imaging, *Nat. Neurosci.* **20**, 327 (2017).
- [17] S. Strand, W. Lutter, J. F. Strasburger, V. Shah, O. Baffa, and R. T. Wakai, Low-cost fetal magnetocardiography: A comparison of superconducting quantum interference device and optically pumped magnetometers, *J. Am. Heart Assoc.* **8**, 013436 (2019).
- [18] P. J. Broser, S. Knappe, D.-S. Kajal, N. Noury, O. Alem, V. Shah, and C. Braun, Optically pumped magnetometers for magneto-myography to study the innervation of the hand, *IEEE Trans. Neural Syst. Rehabil. Eng.* **26**, 2226 (2018).
- [19] I. Savukov, Y. J. Kim, and G. Schultz, Detection of ultralow field NMR signal with a commercial QuSpin single-beam atomic magnetometer, *J. Magn. Reson.* **317**, 106780 (2020).
- [20] M. Limes, E. Foley, T. Kornack, S. Caliga, S. McBride, A. Braun, W. Lee, V. Lucivero, and M. Romalis, Portable Magnetometry for Detection of Biomagnetism in Ambient Environments, *Phys. Rev. Appl.* **14**, 011002 (2020).
- [21] G. Oelsner, R. IJsselsteijn, T. Scholtes, A. Krüger, V. Schultze, G. Seyffert, G. Werner, M. Jäger, A. Chwala, and R. Stolz, Integrated Optically Pumped Magnetometer for Measurements within Earth's Magnetic Field, *Phys. Rev. Appl.* **17**, 024034 (2022).
- [22] J. Iivanainen, R. Zetter, M. Grön, K. Hakkarainen, and L. Parkkonen, On-scalp MEG system utilizing an actively shielded array of optically-pumped magnetometers, *NeuroImage* **194**, 244 (2019).
- [23] E. Boto, N. Holmes, J. Leggett, G. Roberts, V. Shah, S. S. Meyer, L. D. Muñoz, K. J. Mullinger, T. M. Tierney, S. Bestmann, G. R. Barnes, R. Bowtell, and M. J. Brookes, Moving magnetoencephalography towards real-world applications with a wearable system, *Nature* **555**, 657 (2018).
- [24] A. Borna, J. Iivanainen, T. R. Carter, J. McKay, S. Taulu, J. Stephen, and P. D. Schwindt, Cross-axis projection error in optically pumped magnetometers and its implication for magnetoencephalography systems, *NeuroImage* **247**, 118818 (2022).
- [25] S. Pissanetzky, Minimum energy MRI gradient coils of general geometry, *Meas. Sci. Technol.* **3**, 667 (1992).
- [26] D. Budker, W. Gawlik, D. F. Kimball, S. M. Rochester, V. V. Yashchuk, and A. Weis, Resonant nonlinear magneto-optical effects in atoms, *Rev. Mod. Phys.* **74**, 1153 (2002).
- [27] V. I. Yudin, A. V. Taichenachev, Y. O. Dudin, V. L. Velichansky, A. S. Zibrov, and S. A. Zibrov, Vector magnetometry based on electromagnetically induced transparency in linearly polarized light, *Phys. Rev. A* **82**, 033807 (2010).
- [28] W. Happer and B. S. Mathur, Effective operator formalism in optical pumping, *Phys. Rev.* **163**, 12 (1967).
- [29] V. Shah, S. Knappe, P. D. D. Schwindt, and J. Kitching, Subpicotesla atomic magnetometry with a microfabricated vapour cell, *Nat. Photonics* **1**, 649 (2007).
- [30] N. Castagna and A. Weis, Measurement of longitudinal and transverse spin relaxation rates using the ground-state Hanle effect, *Phys. Rev. A* **84**, 053421 (2011).
- [31] J. Dupont-Roc, S. Haroche, and C. Cohen-Tannoudji, Detection of very weak magnetic fields (10^{-9} gauss) by ^{87}Rb zero-field level crossing resonances, *Phys. Lett. A* **28**, 638 (1969).
- [32] C. Cohen-Tannoudji, J. Dupont-Roc, S. Haroche, and F. Laloë, Diverses résonances de croisement de niveaux sur des atomes pompés optiquement en champ nul. I. théorie, *Rev. Phys. Appl. (Paris)* **5**, 95 (1970).
- [33] C. Cohen-Tannoudji, J. Dupont-Roc, S. Haroche, and F. Laloë, Diverses résonances de croisement de niveaux sur des atomes pompés optiquement en champ nul II. applications à la mesure de champs faibles, *Revue de Phys. Appl.* **5**, 102 (1970).
- [34] J. Nurminen, S. Taulu, and Y. Okada, Effects of sensor calibration, balancing and parametrization on the signal space separation method, *Phys. Med. Biol.* **53**, 1975 (2008).
- [35] T. M. Tierney, S. Mellor, G. C. O'Neill, R. C. Timms, and G. R. Barnes, "Spherical harmonic based noise rejection and neuronal sampling with multi-axis OPMs," bioRxiv Publisher: Cold Spring Harbor Laboratory.
- [36] R. M. Hill, E. Boto, M. Rea, N. Holmes, J. Leggett, L. A. Coles, M. Papastavrou, S. K. Everton, B. A. Hunt, D. Sims, J. Osborne, V. Shah, R. Bowtell, and M. J. Brookes, Multi-channel whole-head OPM-MEG: Helmet design and a comparison with a conventional system, *NeuroImage* **219**, 116995 (2020).
- [37] A. Borna, T. R. Carter, J. D. Goldberg, A. P. Colombo, Y.-Y. Jau, C. Berry, J. McKay, J. Stephen, M. Weisend, and P. D. D. Schwindt, A 20-channel magnetoencephalography system based on optically pumped magnetometers, *Phys. Med. Biol.* **62**, 8909 (2017).
- [38] A. Borna, T. R. Carter, A. P. Colombo, Y.-Y. Jau, J. McKay, M. Weisend, S. Taulu, J. M. Stephen, and P. D. D. Schwindt, Non-invasive functional-brain-imaging with an OPM-based magnetoencephalography system, *PLoS ONE* **15**, e0227684 (2020).
- [39] N. Holmes, T. M. Tierney, J. Leggett, E. Boto, S. Mellor, G. Roberts, R. M. Hill, V. Shah, G. R. Barnes, M. J. Brookes, and R. Bowtell, Balanced, bi-planar magnetic field and field gradient coils for field compensation in wearable magnetoencephalography, *Sci. Rep.* **9**, 14196 (2019).
- [40] H. Kutschka, C. F. Doeller, J. Haueisen, and B. Maess, Magnetic field compensation coil design for magnetoencephalography, *Sci. Rep.* **11**, 22650 (2021).
- [41] E. Boto, N. Holmes, J. Leggett, G. Roberts, V. Shah, S. S. Meyer, L. D. Muñoz, K. J. Mullinger, T. M. Tierney, and S. Bestmann, *et al.*, Moving magnetoencephalography towards real-world applications with a wearable system, *Nature* **555**, 657 (2018).
- [42] M. Packer, P. Hobson, N. Holmes, J. Leggett, P. Glover, M. Brookes, R. Bowtell, and T. Fromhold, Planar Coil Optimization in a Magnetically Shielded Cylinder, *Phys. Rev. Appl.* **15**, 064006 (2021).

- [43] J. E. Everett and J. E. Osemeikhian, Spherical coils for uniform magnetic fields, *J. Sci. Instrum.* **43**, 470 (1966).
- [44] A. J. Mäkinen, R. Zetter, J. Iivanainen, K. C. J. Zevenhoven, L. Parkkonen, and R. J. Ilmoniemi, Magnetic-field modeling with surface currents. Part I. Physical and computational principles of BFIELDTOOLS, *J. Appl. Phys.* **128**, 063906 (2020).
- [45] R. Zetter, A. J. Mäkinen, J. Iivanainen, K. C. J. Zevenhoven, R. J. Ilmoniemi, and L. Parkkonen, Magnetic field modeling with surface currents. Part II. Implementation and usage of BFIELDTOOLS, *J. Appl. Phys.* **128**, 063905 (2020).
- [46] V. Shah and M. V. Romalis, Spin-exchange relaxation-free magnetometry using elliptically polarized light, *Phys. Rev. A* **80**, 013416 (2009).
- [47] Z. D. Grujić, P. A. Koss, G. Bison, and A. Weis, A sensitive and accurate atomic magnetometer based on free spin precession, *Eur. Phys. J. D* **69**, 135 (2015).
- [48] D. Hunter, S. Piccolomo, J. D. Pritchard, N. L. Brockie, T. E. Dyer, and E. Riis, Free-Induction-Decay Magnetometer Based on a Microfabricated Cs Vapor Cell, *Phys. Rev. Appl.* **10**, 014002 (2018).
- [49] D. Hunter, R. Jiménez-Martínez, J. Herbsommer, S. Ramaswamy, W. Li, and E. Riis, Waveform reconstruction with a Cs based free-induction-decay magnetometer, *Opt. Express* **26**, 30523 (2018).
- [50] J. Iivanainen, M. Stenroos, and L. Parkkonen, Measuring MEG closer to the brain: Performance of on-scalp sensor arrays, *NeuroImage* **147**, 542 (2017).
- [51] <https://quspin.com/products-qzfm/>.
- [52] O. Alem, R. Mhaskar, R. Jiménez-Martínez, D. Sheng, J. LeBlanc, L. Trahms, T. Sander, J. Kitching, and S. Knappe, Magnetic field imaging with microfabricated optically-pumped magnetometers, *Opt. Express* **25**, 7849 (2017).
- [53] N. V. Nardelli, A. R. Perry, S. P. Krzyzewski, and S. A. Knappe, A conformal array of microfabricated optically-pumped first-order gradiometers for magnetoencephalography, *EPJ Quantum Technol.* **7**, 11 (2020).
- [54] “Twinleaf microSERF OPM,” <https://twinleaf.com/vector/microSERF/>, accessed 2022-01-11.
- [55] E. Edri, N. Armon, E. Greenberg, S. Moshe-Tsurel, D. Lubotzky, T. Salzillo, I. Perelshtein, M. Tkachev, O. Girshevitz, and H. Shpaisman, Laser printing of multilayered alternately conducting and insulating microstructures, *ACS Appl. Mater. Interfaces* **13**, 36416 (2021).
- [56] W. Wu, B. Zhou, Z. Liu, J. Wang, L. Xiaoyang, Y. Jia, and G. Liu, Self-shielded uniform magnetic field coil design for miniature atomic sensors using a particle swarm optimization algorithm, *IEEE Access* **8**, 227866 (2020).
- [57] D. Sheng, S. Li, N. Dural, and M. V. Romalis, Sub-femtotesla Scalar Atomic Magnetometry Using Multipass Cells, *Phys. Rev. Lett.* **110**, 160802 (2013).
- [58] V. G. Lucivero, W. Lee, M. V. Romalis, M. E. Limes, E. L. Foley, and T. W. Kornack, Femtotesla nearly quantum-noise-limited pulsed gradiometer at earth-scale fields (2021), arXiv.
- [59] V. Lucivero, W. Lee, N. Dural, and M. Romalis, Femtotesla Direct Magnetic Gradiometer Using a Single Multipass Cell, *Phys. Rev. Appl.* **15**, 014004 (2021).
- [60] R. J. Clancy, V. Gerginov, O. Alem, S. Becker, and S. Knappe, A study of scalar optically-pumped magnetometers for use in magnetoencephalography without shielding, *Phys. Med. Biol.* **66**, 175030 (2021).